



1 **Characterization of the MISG soot generator with an atmospheric simulation chamber**
2 *Virginia Vernocchi^{1,2}, Marco Brunoldi^{1,2}, Silvia G. Danelli^{1,2}, Franco Parodi², Paolo Prati^{1,2}, Dario*
3 *Massabò^{1,2,*}*

4
5 ¹*Dipartimento di Fisica - Università di Genova, via Dodecaneso 33, 16146, Genova (Italy)*

6 ²*INFN – Sezione di Genova, via Dodecaneso 33, 16146, Genova (Italy)*

7

8 *Correspondence to: D. Massabò (massabo@ge.infn.it)

9

10 **ABSTRACT**

11 The performance of a Mini-Inverted Soot Generator (MISG) has been investigated at ChAMBRé (Chamber
12 for Aerosol Modelling and Bio-aerosol Research) by studying the properties of soot particles generated by
13 ethylene and propane combustion.

14 Starting from an extensive classification of combustion conditions and resulting flame shapes, the MISG
15 exhaust was characterized in terms of concentration of emitted particles and gases, particle size distribution
16 and optical properties. Soot particles were also collected on quartz fibre filters and then analysed by optical
17 and thermal-optical techniques, to measure the spectral dependence of the absorption coefficient b_{abs} , and
18 their composition in terms of Elemental and Organic Carbon (EC and OC). Significant differences could be
19 observed when the MISG is fuelled with ethylene and propane both in terms of particle size and optical
20 behaviour (i.e., absorption coefficient). Values of the Mass Absorption Coefficient (MAC) and of the
21 Angstrom Absorption Exponent (AAE) turned out to be compatible with the literature, even if with some
22 specific difference.

23 The comprehensive characterization of the MISG soot particles is an important piece of information to
24 design and perform experiments in atmospheric simulation chambers.

25

26 **1. Introduction**

27 “Soot” refers to combustion-generated carbonaceous particles that are a by-product of incomplete
28 combustion of fossil fuels and/or biomass burning (Nordmann et al., 2013; Moore et al., 2014). When
29 investigated by optical techniques, soot particles are generally referred as Black Carbon, BC (Petzold et al.
30 2013) while the result of thermal - optical characterizations is referred as Elemental Carbon, EC, (Bond and
31 Bergstrom, 2006). However, both BC and EC are defined in operative terms that do not identify the same
32 compounds (Massabò and Prati, 2021) and often produce non-negligible differences in concentration values.

33 Soot particles constitute an important fraction of anthropogenic particulate matter (PM) especially in urban
34 environments (Weijer et al. 2011), and are emitted by traffic, domestic stoves, industrial chimneys and by any
35 incomplete combustion process.

36 Several works state adverse effects of soot both on climate (Ackerman et al., 2000; Menon et al., 2002;
37 Quinn et al., 2008; Ramanathan and Carmichael, 2008; Bond et al., 2013) and health (Pope et al., 2002;
38 Anenberg et al., 2010; Gan et al., 2011; Cassee et al., 2013; Lelieveld et al., 2015). From the climatic point of
39 view, soot particles absorb the solar radiation, causing a positive radiative forcing. Effects on health include
40 cardiopulmonary morbidity and mortality (Janssen et al., 2012). The understanding of properties and behaviour
41 of soot particles when they are suspended in the atmosphere is thus necessary to fully assess their adverse
42 effects and the use of proxies with controlled and known properties can be useful.

43 So far, soot generators have been employed for studies on optical properties (Zhang et al. 2008; Cross et
44 al. 2010; Mamakos et al. 2013; Utry et al. 2014 b; Bescond et al. 2016), instruments calibration (Onasch et al.
45 2012; Durdina et al. 2016) and several other purposes (Pagels et al. 2009; Henning et al. 2012; Ghazi et al.
46 2013; Ghazi and Olfert 2013). The Inverted-Flame Burner (Stipe et al. 2005) is often considered as an ideal
47 soot source (Moallemi et al., 2019 and references therein), due to its capacity to generate almost pure-EC
48 particles and for the stability of the flame and of its exhaust (Stipe et al. 2005). To such category belongs the



49 Mini-Inverted Soot Generator, MISG (Argonaut Scientific Corp., Edmonton, AB, Canada, Model MISG–2),
50 used in this work.

51 The MISG can be operated with different fuels: ethylene (Kazemimanesh et al., 2019), propane (Moallemi
52 et al., 2019), and theoretically also with ethane or fuel blends with methane and nitrogen, even if, to our
53 knowledge, no literature is available on such configurations. The air to fuel flow ratio can be adjusted to control
54 concentration and size of the generated particles. The maximum reachable concentration is about 10^7 particles
55 cm^{-3} (<https://www.argonautscientific.com/>), while particle size ranges from few tens to few hundreds of nm.

56 The behaviour of soot particles can be efficiently studied in/by atmospheric simulation chambers (ASCs):
57 these are exploratory platforms which allow to study atmospheric processes under controlled conditions, that
58 can be maintained for periods long enough to reproduce realistic environments and to study interactions among
59 their constituents (Finlayson - Pitts and Pitts, 2000; Becker, 2006). Recent examples concern the investigation
60 of the optical properties of mineral dust (Caponi et al., 2017) and wood-burning exhausts (Kumar et al., 2018).

61 Coupling the MISG to an ASC makes possible systematic experiments on the properties of soot particles
62 exposed and maintained in different conditions. In this work we mainly investigated the differences between
63 MISG exhausts produced by ethylene and propane burning.

64

65 2. Materials and methods

66

67 2.1 Mini-Inverted Soot Generator

68 The MISG, introduced by Kazemimanesh (2019), is a combustion-based soot generator working as an
69 inverted-flame burner (Stipe et al., 2005) where air and fuel flow in an opposite way to the buoyancy force of
70 the hot exhaust gases. This results in a co-flow diffusion flame and leads to a better flame stability by reducing
71 flame tip flickering (Kirchstetter & Novakov, 2007; Stipe et al., 2005) and consequently to a more stable soot
72 particle generation.

73 The MISG is fed with air and fuel supplied by specific cylinders: we used both ethylene and propane, two
74 fuels with a well-known capability of producing soot. Air and fuel flow rates are controlled by two mass flow
75 controllers (MFCs, Bronkhorst High-Tech B.V., Ruurlo, Netherlands, Models F-201CV-10K-MGD-22-V and
76 FG-201CV-MGD-22-V-AA-000, respectively) operated via a home-made National Instruments Labview
77 code. The air and fuel flows can be controlled in the range 0–12 lpm and 0–200 mlpm, respectively. Differently
78 from other commercial generators, the MISG does not require a third gas (i.e., N_2) used as a carrier and the air
79 flow is internally split between combustion and carriage operations. This implies that the ratio of comburent
80 and carrier gas is not controllable, and the user can only adjust the comburent to fuel ratio.

81 The efficiency of the combustion process can be given in terms of the global equivalence ratio, starting
82 from the air-to-fuel ratio (AFR):

83

$$84 \quad AFR = \frac{m_A}{m_F} = \frac{n_A * M_A}{n_F * M_F}$$

85 where:

86 m_A : air mass;

87 m_F : fuel mass;

88 n_A : number of air moles;

89 n_F : number of fuel moles;

90 M_A : air molecular weight;

91 M_F : fuel molecular weight.

92



93 The stoichiometric AFR value is $15.64 \text{ m}^3 \text{ m}^{-3}$ (inverse value = $0.064 \text{ m}^3 \text{ m}^{-3}$) and $14.75 \text{ m}^3 \text{ m}^{-3}$ (inverse value
94 = $0.068 \text{ m}^3 \text{ m}^{-3}$), for propane and ethylene, respectively. Finally, the ratio between stoichiometric and actual
95 AFR corresponds to the global equivalence ratio:

96

$$97 \quad \varphi = \frac{(m_F / m_A)}{(m_F / m_A)_{st}}$$

98

99 where:

100 (m_F/m_A) : inverse of actual AFR;

101 $(m_F/m_A)_{st}$: inverse of stoichiometric AFR.

102

103 The flame is classified as fuel-rich and fuel-lean when $\phi > 1$ and $\phi < 1$, respectively. It is yet demonstrated
104 (Moore et al., 2014) that fuel-lean flames produce soot particles with larger mode diameter (about 100-200
105 nm) while fuel-rich flames lead to an additional mode in the nucleation size range (i.e., 10-30 nm). Finally,
106 Mamakos (2013) reported that low fuel-to-air ratios (i.e., $\phi < 1$) generate particles with a large fraction of EC
107 while semi-volatile organics are generated by high fuel-to-air ratios (i.e., $\phi > 1$). In this work, fuel-lean
108 conditions were investigated only.

109 Since the combustion process can produce flame shapes having different characteristics, we first explored
110 the range of combustion flows from 2 to 10 lpm, in 0.5 lpm steps, and from 30 to 100 mlpm, in 5 mlpm steps,
111 respectively for air and fuel. Flame types can be distinguished (Kazemimanesh et al., 2019; Moallemi et al.,
112 2019) as:

113 - *Closed tip* flame (Fig. 1.a), which generates low concentrations of soot particles (i.e., around $10^3 \# \text{ cm}^{-3}$),
114 generally forming particle aggregates at the nozzle of the MISG.

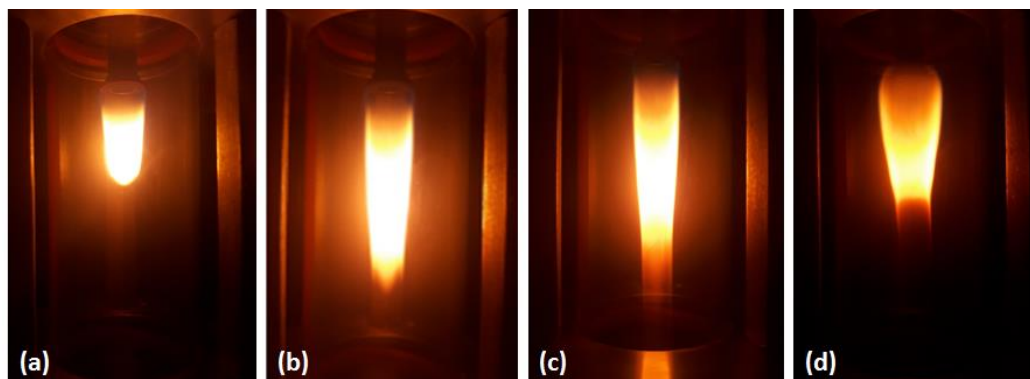
115 - *Partially Open tip* flame (Fig. 1.b), the transition between *Open* and *Closed tip*.

116 - *Open tip* flame (Fig. 1.c), which generates high concentrations of soot particles (i.e., $> 10^5 \# \text{ cm}^{-3}$).

117 - *Asymmetric* flame, which shows a large variability (very short, flickering, etc) and can form particle
118 aggregates at the MISG nozzle.

119 - *Curled Base* flame (Fig. 1.d), a particular shape of the asymmetric flames that can also form particles
120 aggregates at the MISG nozzle.

121



123 *Figure 1: Examples of different flame shapes: (a) Closed tip, (b) Open tip, (c) Partially Open tip, (d) Curled base flame.*

124

125 By the flames observation (Sect. 2.1.2), we selected the more interesting combustion conditions (i.e., *Open*
126 *tip* flames) to perform the characterization experiments. We focused on *Open tip* flames because it is the flame
127 that generates higher concentrations of soot particles. Operative conditions selected for propane and ethylene



128 combustion are reported in Tables 1 and 2: we maintained the same air flow and global equivalence ratio with
129 both the fuels.

130

Table 1: Combustion parameters and flame shapes selected for propane.

PROPANE			
AIR flow [lpm]	FUEL flow [mlpm]	Global Equivalence Ratio	Flame shape
7	70	0.244	Partially Open Tip
7	75	0.261	Open Tip
7	80	0.278	Open Tip
7	85	0.296	Open Tip
8	70	0.213	Partially Open Tip
8	75	0.228	Open Tip
8	80	0.244	Open Tip
8	85	0.259	Open Tip

131
132
133
134

Table 2: Combustion parameters and flame shapes selected for ethylene.

ETHYLENE			
AIR flow [lpm]	FUEL flow [mlpm]	Global Equivalence Ratio	Flame shape
7	118	0.244	Partially Open Tip
7	127	0.261	Open Tip
7	135	0.278	Open Tip
7	144	0.296	Open Tip
8	118	0.213	Partially Open Tip
8	127	0.228	Open Tip
8	135	0.244	Open Tip
8	144	0.259	Open Tip

135
136
137
138

2.2 Chamber setup

139 Experiments took place at the ChAMBRe (Chamber for Aerosol Modelling and Bio-aerosol Research)
140 facility (Massabò et al., 2018; Danelli et al., 2021) located at the Physics Department of the University of
141 Genoa.

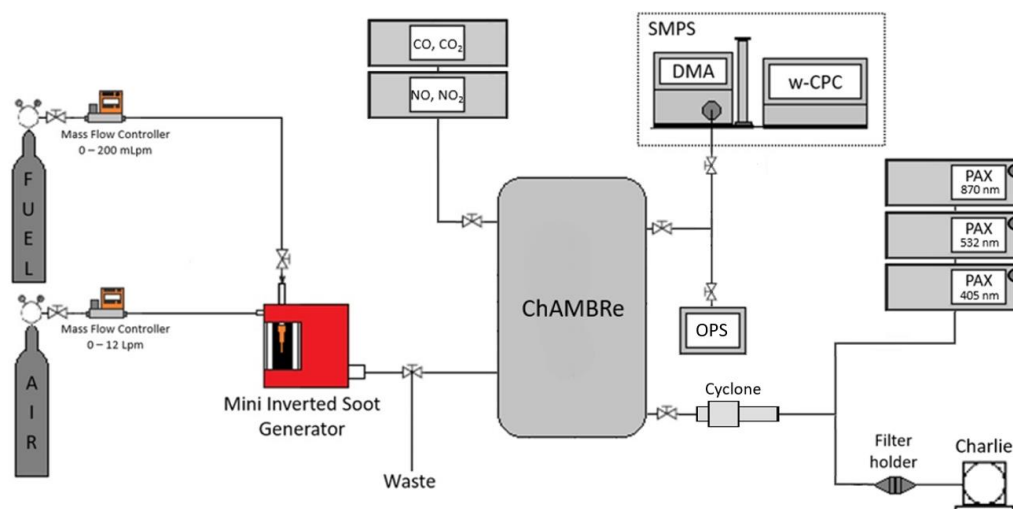


142 ChAMBRe is a stainless-steel chamber, with a volume of about 2.2 m³. Inside the chamber, relative
143 humidity, temperature, and pressure are continuously monitored by a HMT334 Vaisala® Humicap®
144 transmitter and a MKS Instruments 910 DualTrans™ transducer, respectively. Two gas analyzers from
145 Environnement SA, continuously monitored the concentration of NO/NO₂ (model: AC32e), and CO/CO₂
146 (model: CO12e) inside the chamber or, alternatively, in the laboratory. The mixing of gas and aerosol species
147 is favoured by a fan installed in the bottom of the chamber: mixing time for gaseous species is of about 180 s
148 with a fan rotating speed of 1.6 revolutions per second. A composite pumping system (rotary pump TRIVAC®
149 D65B, Leybold Vacuum, root pump RUVAC WAU 251, Leybold Vacuum and Leybold Turbovac 1000)
150 allows to evacuate the internal volume down to 10⁻⁵ mbar; in this way ChAMBRe is cleaned before each
151 experiment. Before and during the experiments, ambient air enters the chamber throughout a 5-stage
152 filtering/purifying inlet (including a HEPA filter, model: PFIHE842, NW25/40 Inlet/Outlet – 25/55 SCFM,
153 99.97 % efficient at 0.3 μm). The whole set-up is managed by a custom NI Labview SCADA (Supervisory
154 Control And Data Acquisition).

155 The layout of the experimental configuration adopted for the MISG characterization is shown in Fig. 2.

156 The MISG was warmed for about 45 minutes before injecting soot particles inside the chamber. Injection
157 of soot particles inside ChAMBRe lasted 2 or 3 minutes, depending on the soot concentration required for each
158 experiment. We performed some fluid dynamic evaluations with the Particle Loss Calculator software tool
159 (PLC; von der Weiden et al., 2009). The geometry of our experimental setup, combined with particle size and
160 used flow rates, resulted in particle losses lower than 0.1 % in the dimensional range of 80-2000 nm. All the
161 experiments were performed at atmospheric pressure, 19° < T < 21 °C and R.H. < 50 %.

162



163

164 *Figure 2: Layout of the MISG set-up at ChAMBRe.*

165

166 2.3 Size distributions

167 Particle concentration and size distribution inside the chamber were measured by a scanning mobility
168 particle sizer (SMPS, TSI Inc., Shoreview, MN, USA, Model 3938), composed by a differential mobility
169 analyzer (DMA, TSI Inc., Shoreview, MN, USA, Model 3081A) and a water condensation particle counter
170 (w-CPC, TSI Inc., Shoreview, MN, USA, Model 3789). The water-CPC is filled using technical demineralized
171 water (Conductivity (20°C), max. 1.5 μS/cm; VWR Chemicals INTERNATIONAL S.R.L.). The SMPS was



172 set to measure particles with mobility diameter from 34 nm to 649 nm; aerosol sample and sheath airflow rates
173 were fixed at 0.17 lpm and 1.60 lpm, respectively, while the scanning period for each cycle was 70 s. The
174 DMA unit integrates an impactor with an orifice of 0.0508 cm, resulting in cut-off capability at 50 % of 940
175 nm, useful to exclude all the particles larger than this size to enter in the column. Frequent cleaning of this part
176 was necessary to ensure proper operation and avoid clogging; at the end of each experiment, the whole
177 impactor system was cleaned using compressed air and isopropyl alcohol.

178 We corrected diffusion losses in the instrument by using the option included in the instrument software;
179 size distributions were as well corrected for multiple charges effects through the TSI proprietary software
180 (Aerosol Instrument Manager, Version 11-0-1).

181 Among the other chamber instruments, an Optical Particle Sizer (OPS, TSI Inc., Shoreview, MN, USA,
182 Model 3330) was used for short times to spot the particle size distribution in the range 0.3-10 μm .

183

184 **2.4 Online optical measurements**

185 Three photoacoustic extinction-meters (PAXs, Droplet Measurement Technologies, Boulder, CO, USA)
186 were deployed, providing the online determination of the soot particles absorption coefficients at $\lambda = 870, 532$
187 and 405 nm. PAXs are constituted by a measurement cell where aerosol optical properties are measured by
188 two different mechanisms (<https://www.dropletmeasurement.com/>, PAX Operator Manual). The sample flow
189 rate (1 lpm) is split in two different sectors of the cell, both crossed at the same time by the light of a modulated
190 laser diode. In the absorption sector, soot particles absorb light and release acoustic waves which are then
191 detected by an ultra-sensitive microphone. The intensity of the acoustic signal is interpreted to infer the particle
192 absorption coefficient. In the other sector, a wide angle reciprocal nephelometer measures the scattering
193 coefficient instead. It is noteworthy that no correction for the truncation angle is applied by the manufacturer:
194 this can lead to substantial underestimation of the scattering coefficient, which generally grows as the particle
195 size increases and the single scattering albedo (SSA) approaches unity. However, since particles produced by
196 soot generators have dimensions much lower than 1 μm and SSA values lower than 0.3 (Moallemi et al., 2019),
197 we disregarded this issue. The PAXs had been calibrated by the manufacturer.

198 In some experiments, soot concentration inside the chamber was too high to be measured directly by PAXs;
199 and a diluter (eDiluter Pro, Dekati Ltd., Kangasala, Finland) was deployed. Dry air from a cylinder was merged
200 prior to the PAXs inlet with dilution factor 1:100. Tests performed with and without the diluter demonstrated
201 a substantial reproducibility of the optical properties measured by the PAXs when the proper dilution factor is
202 considered.

203

204 **2.5 Offline analysis**

205 Soot particles were also collected on pre-fired 47 mm diameter quartz fibre filters (Pallflex Tissuquartz
206 2500 QAO-UP) held in a stainless-steel filter holder to allow additional offline analysis. The sampling started
207 when stable gas and particle concentration values were reached inside the chamber (i.e., about 3 minutes -
208 corresponding to the chamber mixing time - after the MISG switching off): for each working condition three
209 filters with different loadings were obtained by a low-volume sampler (TECORA – Charlie HV) working at a
210 fixed sampling flow (i.e., 10 lpm during experiments without cyclone and 13.67 lpm during experiments with
211 cyclone).

212 For each sample, the EC and OC mass concentration was determined by thermal-optical transmittance
213 analysis (TOT) using a Sunlab Sunset EC/OC analyzer and the NIOSH5040 protocol (NIOSH, 1999),
214 corrected for temperature offsets.

215 Prior to EC/OC determination, particle-loaded filters were analyzed by the Multi-Wavelength Absorbance
216 Analyzer (MWAA, Massabò et al., 2013 and 2015), a laboratory instrument for the offline direct quantification
217 of the aerosol absorption coefficients at five different wavelengths ($\lambda = 850, 635, 532, 405$ and 375 nm). Such
218 peculiar feature had been previously exploited in the frame of several field campaigns in urban and rural sites



219 (Scerri et al., 2018; Massabo et al, 2019; Massabo et al, 2020; Moschos et al., 2021), as well as in peculiar and
220 remote sites (Massabo et al., 2016; Saturno et al., 2017; Baccolo et al., 2021).

221

222 **2.6 Cyclone experiments**

223 Soot aggregates are also generated by the MISG. Kazemimanesh (2019) retrieved super-aggregates larger
224 than 2 μm for ethylene combustion while Moallemi (2019) showed aggregate structures larger than 1 μm with
225 propane. On this basis, confirmed by some short checks by the OPS, we replicated each experiment (see Sect.
226 2.1) both without and with a cyclone (PM1 Sharp Cut Cyclone - SCC 2.229, MesaLabs, Lakewood, CO, USA)
227 inserted upstream the PAXs and filters sampler (Fig. 2). The cyclone has a cut-off of 1 μm at a nominal flow
228 of 16.66 lpm.

229

230 **3. Results and Discussion**

231 **3.1 Characterization tests**

232 The categories of flame shape observed in the range of air and fuel flows discussed in sect. 2.1.2 are
233 summarized in Tables 3 and 4, for propane and ethylene respectively. The MISG characterization with propane
234 has been previously published (Moallemi et al., 2019) and we used it as reference. We got some differences
235 especially in the range of transition from *Closed tip* to *Open tip*, probably due to the different setups. Fuel
236 flows higher than 85 mlpm were not investigated due to instrumental limitation. To our knowledge, no
237 literature information is available for the ethylene in the flow range of Table 4. It is noteworthy that no
238 correlation could be found between the global equivalence ratio (ϕ) and the shape of the corresponding flame.
239 This means that the fundamental parameter of the combustion process can not be used to predict the flame
240 shape.

241 The reproducibility and stability of the MISG emissions were investigated, in terms of number
242 concentration and size distribution of the generated soot particles. Different combustion conditions were
243 selected, and four experiments were performed for each combination of air and fuel flows. We chose to keep
244 fixed the air flow to observe the differences produced by different fuel flows that correspond to different flame
245 shapes (i.e., *Partially Open tip* or *Open tip*). In each test, we recorded the values of total particle number
246 concentration, peak concentration, and mode diameter. The reproducibility was calculated as the percentage
247 ratio between standard deviation and mean value of each series of repeated experiments. With propane, mode
248 reproducibility turned out to be 6 %, while total concentration and peak concentration showed a 16 %
249 reproducibility. With ethylene, the reproducibility was 4 % and 10 %, respectively for mode and total/peak
250 concentration. In addition, we monitored the combustion gases: CO₂ and NO concentration varied by about 2
251 % and 3 %, respectively with propane and ethylene.

252

253 *Table 3: Flame shapes observed for different combustion conditions of propane. Flames are identified as A - asymmetric,*
254 *CB - Curled Base, CT - Closed tip, POT - Partially Open tip and OT - Open tip; FL indicates if flickering. The dash*
255 *indicates that the flame does not ignite.*



		FUEL flow [mlpm]												
		30	35	40	45	50	55	60	65	70	75	80	85	
AIR flow [lpm]	2	A	A/FL	A	A/FL	A	CB/FL	CB/FL	CB/FL	CB/FL	CB/FL	CB/FL	CB/FL	CB/FL
	2.5	A/FL	A/FL	A	A/FL	A/FL	CB/FL	CB/FL	CB/FL	CB/FL	CB	CB	CB/FL	
	3	A/FL	A/FL	A	A/FL	A/FL	CB/FL	CB/FL	CB/FL	CB/FL	CB/FL	CB	CB/FL	
	3.5	A/FL	A	A	A	A	CB	CB	CB	CB	CB	CB	CB/FL	
	4	A	A	A	A	A	CB	CB	CB/FL	CB	CB	CB	OT	
	4.5	A	A	A	A	A	CB	CB	CB	CB	CB	CB	OT	
	5	A	A	A	A	A	A/CB	CT	POT	OT	OT	OT	OT	
	5.5	A	A	A	A	A	CT	CT	POT	OT	OT	OT	OT	
	6	A	A	A	A	CT	CT	CT	CT	POT/OT	OT	OT	OT	
	6.5	A	A	A	A	CT	CT	CT	CT	POT	OT	OT	OT	
	7	A	A	A	A	A	CT	CT	CT	POT	POT/OT	OT	OT	
	7.5	A	A	A	A	A	CT	CT	CT	POT	POT/OT	OT	OT	
	8	-	-	A	A	A	CT	CT	CT	POT	POT/OT	OT	OT	
	8.5	-	-	A	A	A	CT	CT	CT	POT/OT	POT/OT	OT	OT	
	9	-	-	A	A	A	CT	CT	CT	CT	POT	OT	OT	
9.5	-	-	-	A	A	CT	CT	CT	CT	POT	OT	OT		
10	-	-	-	A	A	CT	CT	CT	CT	POT	OT	OT		

256

257

258

259

260

Table 4: Flame shapes observed for different combustion conditions of ethylene. Flames are identified as A - asymmetric, CB - Curled Base, CT - Closed tip, POT - Partially Open tip and OT - Open tip; FL indicates if flickering.

		FUEL flow [mlpm]														
		30	35	40	45	50	55	60	65	70	75	80	85	90	95	100
AIR flow [lpm]	2	A	A	A	A	A/FL	A	A	A	CB	CB	CB	CB	CB	CB	CB
	2.5	A	A	A	A/FL	A/FL	A/FL	A	A	CB	CB	CB	CB	CB	CB	CB
	3	A	A	A	A	A/FL	A/FL	A	A	A/CB	CB	CB	CB	CB	CB	CB
	3.5	A	A	A	A	A/FL	A/FL	A	A	A/CB	CB	CB	CB	CB	CB	CB
	4	A	A	A	A	A	A	A	A	A	A/CB	CB	CB	CB	CB	CB/OT
	4.5	A	A	A	A	A	A	A	A	CB	CB	CB	CB	CB/OT	CB/OT	CB/OT
	5	A	A	A	A	A	A	A	A	CB	CB	CB	CB	CB/OT	CB/OT	CB/OT
	5.5	A	A	A	A	A	A	A	A	CB	CB/OT	CB/OT	CB/OT	CB/OT	CB/OT	CB/OT
	6	A	A	A	A	A	A	CT	CT	CT	CT/POT	CT/POT	POT	POT	OT	OT
	6.5	A	A	A	CT	CT	CT	CT	CT	CT/POT	POT	POT/OT	POT/OT	OT	OT	OT
	7	A	A	A	CT	CT	CT	CT	CT/POT	POT	POT/OT	OT	OT	OT	OT	OT
	7.5	A	A	A	A	CT	CT	CT	CT	POT	POT/OT	OT	OT	OT	OT	OT
	8	A	A	A	CT	CT	CT	CT	CT/POT	POT	POT/OT	OT	OT	OT	OT	OT
	8.5	A	A	A	CT	CT	CT	CT	CT	CT/POT	POT	OT	OT	OT	OT	OT
	9	A	A	CT	CT	CT	CT	CT	CT	POT	OT	OT	OT	OT	OT	OT
9.5	A	A	CT	CT	CT	CT	CT	CT	CT	POT	OT	OT	OT	OT	OT	
10	A	CT	CT	CT	CT	CT	CT	CT/POT	POT	POT/OT	OT	OT	OT	OT	OT	

261

262

263



264 3.2 Comparison between propane and ethylene exhausts

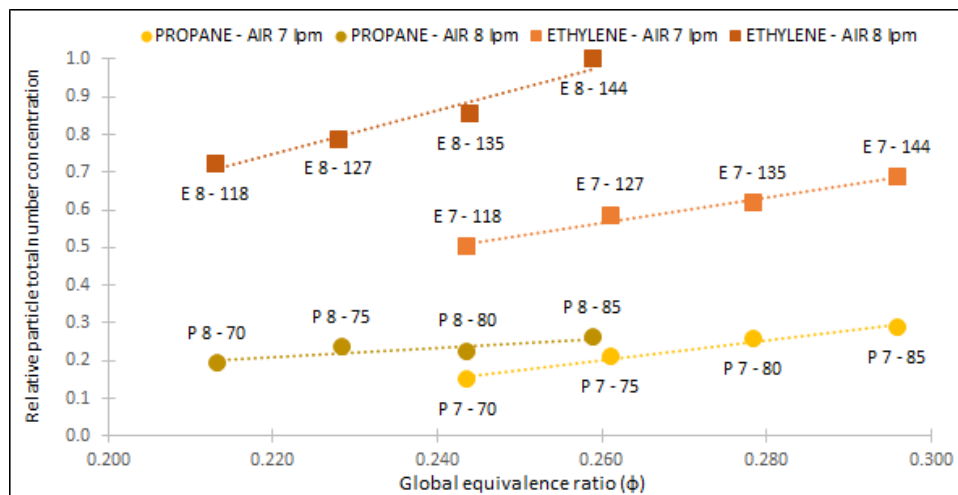
265 Previous works investigated concentration and mode of ethylene (Kazemimanesh et al., 2019) propane
266 (Moallemi et al., 2019) fuelled MISG exhausts. We expand here to a detailed comparison between the two
267 fuels, focusing on ASC experiments.

268 3.2.1 Size distribution

269 To compare different experiments, particle concentration values were normalized to the maximum recorded
270 in the whole set of tests and therefore varied in the 0-1 range. Fig. 3 shows the result for the total particle
271 number concentration, we can notice that:

- 272 - At fixed air flow, the particle number concentration increases with the fuel flow (i.e., with the global
273 equivalence ratio).
- 274 - In the same combustion conditions (i.e., same air flow and same global equivalence ratio), ethylene generates
275 more particles than propane.
- 276 - With ethylene and at fixed fuel flow, the particle number concentration increases with the air flow. The same
277 holds in some cases with propane but with much smaller variations.

278

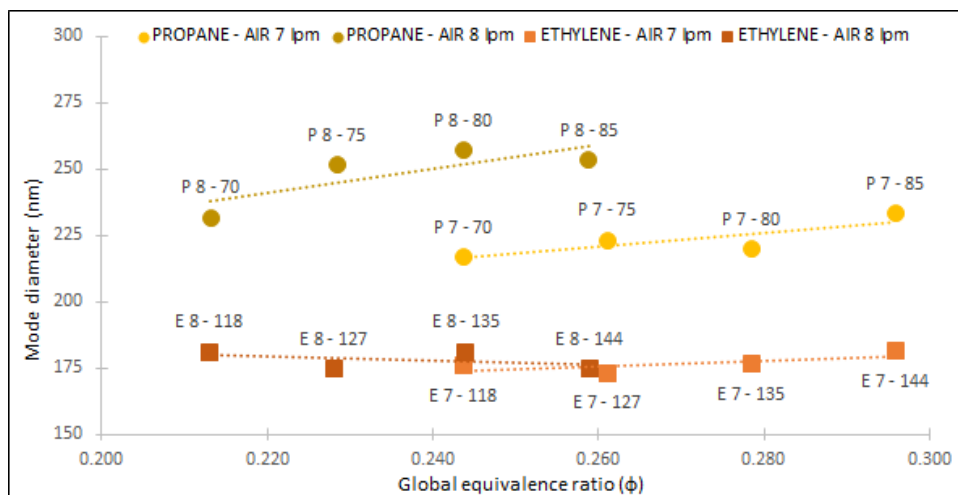


279

280 Figure 3: Particle number concentration vs the global equivalence ratio. Values are normalized to the highest of the
281 whole set. Each point is labelled by E or P (ethylene or propane) and a pair of numbers indicating air and fuel flow rate,
282 respectively in lpm and mlpm.

283

284 A similar comparison is shown in Fig. 4 for the particle mode diameter: while the values are basically constant
285 for ethylene, the mode diameter with propane slightly increases with air flow (at fixed fuel flow). Furthermore,
286 at each ϕ value, propane generated particles bigger than ethylene.



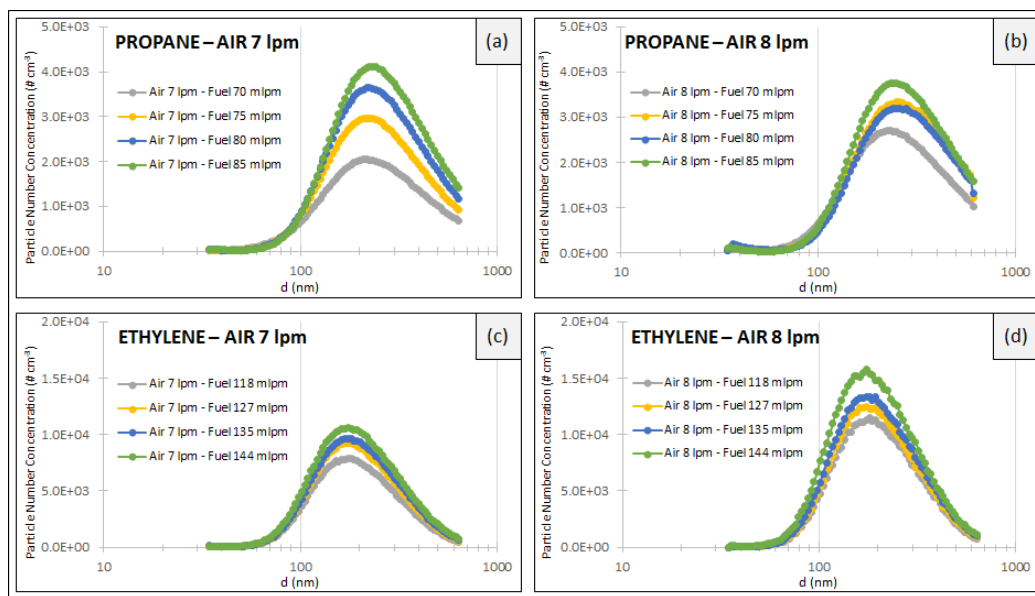
287

288 *Figure 4: Mode diameter versus the global equivalence ratio. Each point is indicated by E or P (ethylene or propane)*
289 *and a pair of numbers indicating air and fuel flow rate, respectively in lpm and mlpm.*

290
291

292 Both in (Kazemimanesh et al., 2019) with ethylene and (Moallemi et al., 2019) and (Bischof et al., 2019)
293 with propane, when the fuel flow increased, at a certain air flow, the particle number concentration increased
294 too; even if a lower range of global equivalence ratio were considered. In addition, Kazemimanesh (2019) and
295 Bischof (2019) also reported that the particle mode diameter, both with ethylene and propane, did not depend
296 on the global equivalence ratio, as we also observed. In (Moallemi et al., 2019), instead, they observed an
297 opposite behaviour for mode diameters: they retrieved that at fixed fuel flow, a higher air flow produced a
298 slight decrease of the mode diameter. Both (Moallemi et al., 2019) and (Bischof et al., 2019) measured mode
299 diameters < 200 nm, but this can be due to the specific combustion conditions (i.e., lower global equivalence
300 ratios resulting from higher air flow or lower fuel flow).

301 The mean size distributions observed at ChAMBre are given in Fig. 5, for all the selected operative
302 conditions. All the curves are normalized to the same injection time (i.e., 3 min).



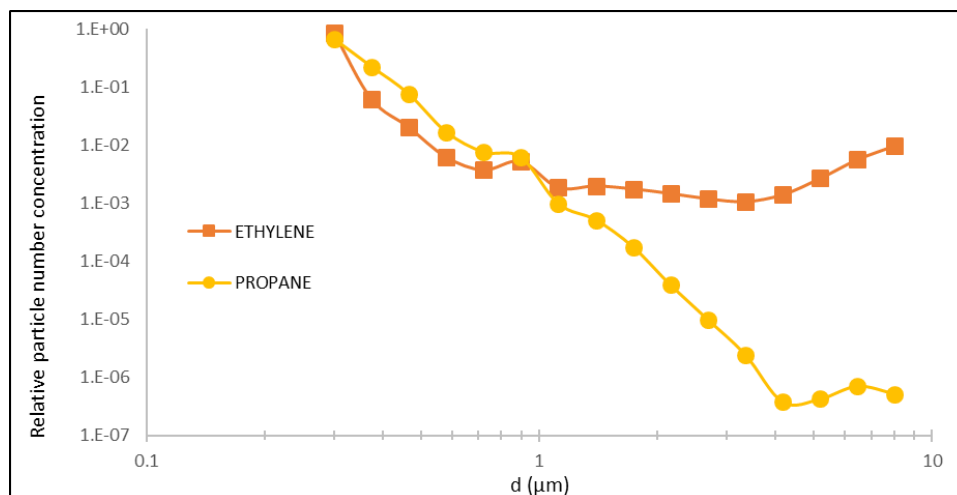
303

304 *Figure 5: Mean size distributions measured by SMPS. MISG was fuelled with propane (top panels) and ethylene (bottom*
305 *panels) with the air and fuel flows indicated in the plots frame.*

306

307 Significant differences between the two fuels emerge when considering the particle mass concentration
308 (extended to 10 μm , including the data collected by the OPS): ethylene combustion produced a limited number
309 of big particles, likely super-aggregates, formed directly at the MISG exhaust. Kazemimanesh (2019) also
310 observed the formation of aggregates, even with smaller dimensions (i.e., about 2 μm). We calculated the
311 super-micrometric fraction of the total measured by the OPS with both the fuel (Fig. 6): this resulted to be
312 about 3% with ethylene and 0.2% with propane. Particles larger than 4 μm were about 2% with ethylene, with
313 a peak at 8 μm , and totally negligible with propane. Considering the particle volume distribution, the latter
314 difference is obviously enhanced: the super-micrometric fraction is about 99% of the total concentration with
315 ethylene and 9% only with propane. Particles larger than 4 μm contribute to the total volume (and hence to the
316 soot concentration) for about 98% and 1%, respectively with ethylene and propane.

317



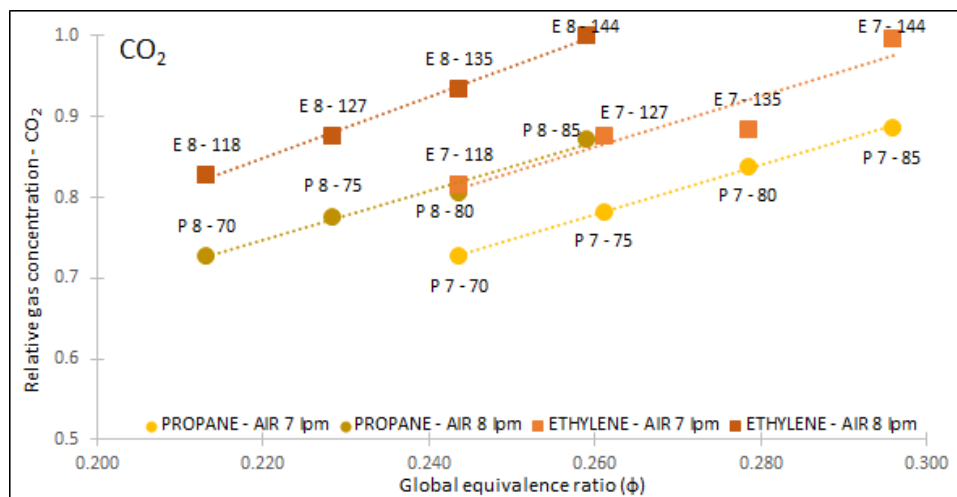
318

319 *Figure 6: Relative particle number concentration normalized to the total number concentration of particles, in function*
 320 *of particle size, measured by OPS.*

321

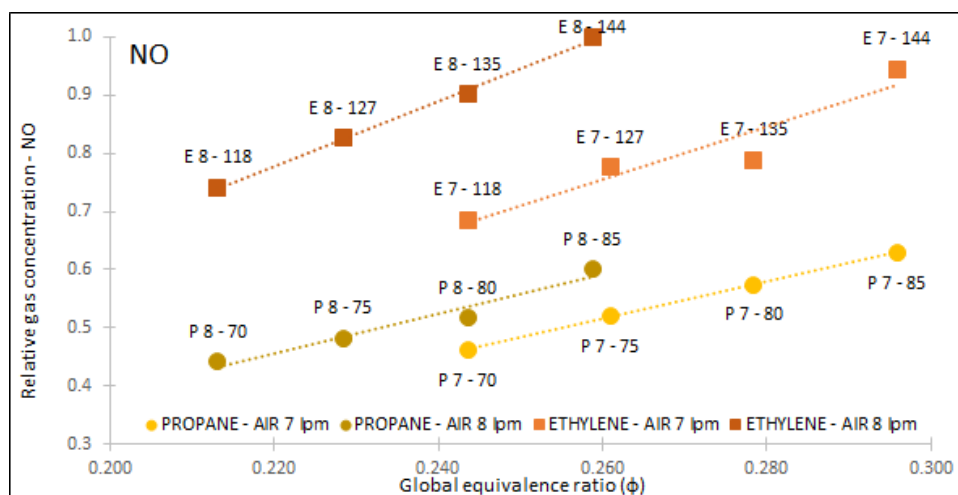
3.2.2 Gaseous exhaust

322 Gaseous emissions were characterized too, focusing on the most abundant gases i.e., CO₂ and NO. The
 323 pattern is similar for both the gases: at fixed air flow rate, gas concentration increased with the fuel flow while
 324 no significant differences emerged at fixed fuel flow rate and changing the air flow. At equal operative
 325 conditions (i.e., same combustion conditions, injection time and time from the injection), gaseous emissions
 326 were higher with ethylene than with propane. With the same normalization introduced in Fig. 3, the CO₂ and
 327 NO production are compared in Fig. 7 and 8 for each selected MISG configuration. Maximum values were
 328 360 ppm and 980 ppb, respectively for CO₂ and NO, after 3 minutes of soot injection.
 329



330

331 *Figure 7: CO₂ concentration versus the global equivalence ratio. Each value was normalized to the highest of the whole*
 332 *set. Data points are labelled by E or P (ethylene or propane) and a pair of numbers indicating air and fuel flow,*
 333 *respectively in lpm and mlpm.*



334

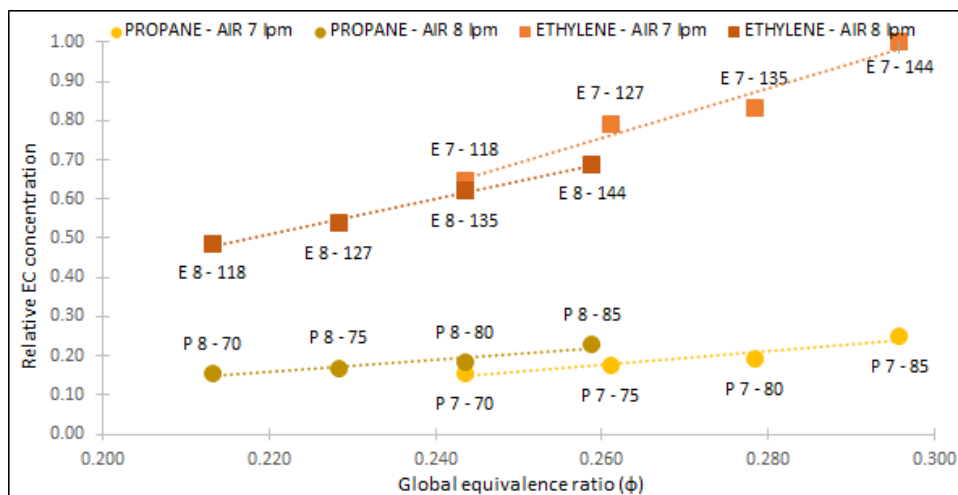
335 *Figure 8: NO concentration versus the global equivalence ratio. Each value was normalized to the highest of the whole*
336 *set. Data points are labelled by E or P (ethylene or propane) and a pair of numbers indicating air and fuel flow,*
337 *respectively in lpm and mlpm.*

338

339 3.2.3 EC/OC quantification

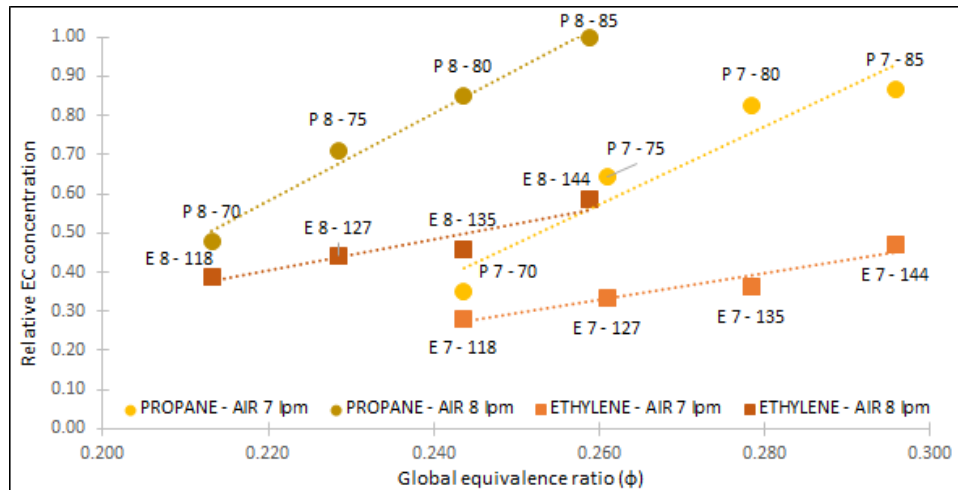
340 The OC/EC composition was quantified by thermal-optical analysis of samples collected on quartz fibre
341 filters during each experiment. EC:TC concentration ratios resulted to be around 0.7 and 0.9 with propane and
342 ethylene, respectively. In addition, the EC:TC concentration ratios increased with the global equivalence ratio.
343 All the results are given in Fig. 9 and 10, for experiments without and with cyclone respectively, adopting the
344 same normalization already introduced in Fig. 3. When removing large particles (see Sect 3.2.1), the EC:TC
345 concentration ratio resulted higher with propane (0.83 against 0.79 measured with ethylene). Actually, with
346 ethylene about 40 % of the EC concentration was associated with particles larger than 1 μm . With both fuels,
347 EC:OC ratios increase with the global equivalence ratios whether the cyclone is present or not, in agreement
348 with (Kazemimanesh et al., 2019) and (Moallemi et al., 2019).

349



350

351 Figure 9: EC mass concentration versus the global equivalence ratio, each value was normalized to the highest of the
 352 whole set. Each point is labelled by E or P (ethylene or propane) and a pair of numbers indicating air and fuel flow rate,
 353 respectively in lpm and mlpm. No cyclone.
 354



355

356 Figure 10: EC mass concentration versus the global equivalence ratio, each value was normalized to the highest of the
 357 whole set. Each point is labelled by E or P (ethylene or propane) and a pair of numbers indicating air and fuel flow rate,
 358 respectively in lpm and mlpm. The cyclone impactor upstream the filter removed super-micrometric particles.
 359

360 The OC:EC ratio varies from 0.31 for propane to 0.19 and 0.10 for ethylene, with and without cyclone
 361 respectively. In each series of experiments (i.e., air flow rate 7 or 8 lpm, ethylene or propane) the OC fraction
 362 turned out to be inversely proportional to the fuel flow with a minimum at the lowest fuel flow (i.e., 70 lpm
 363 with propane and 118 lpm with ethylene). This is likely due to the shape of the flame: flames generated by the
 364 lowest fuel flow conditions are *Partially Open tip*, with less capability to generate soot particles and hence EC;
 365 so that the EC:OC ratio results lower.

366 We also performed some tests adding a backup filter during the sampling to catch the volatile fraction of
 367 OC. The OC concentration values measured on backup filters showed high variability, but they were
 368 compatible with those on not-sampled filters. We analysed 13 blank filters from different bunches and the



369 average concentration of OC resulted $\langle \text{OC} \rangle = 0.5 \pm 0.2 \mu\text{g cm}^{-2}$ while OC concentration on backup filters was
370 $\langle \text{OC}_{\text{BF}} \rangle = 0.6 \pm 0.2 \mu\text{g cm}^{-2}$ (average OC concentration on the corresponding main filters was $1.4 \pm 0.7 \mu\text{g}$
371 cm^{-2}). A relationship between OC concentration on the backup filter and the global equivalence ratio was
372 instead reported in (Kazemimanesh et al., 2019). Actually, in that study the range of investigated global
373 equivalence ratio values was $0.129 < \phi < 0.186$ to be compared $\phi > 0.210$ adopted in this work.

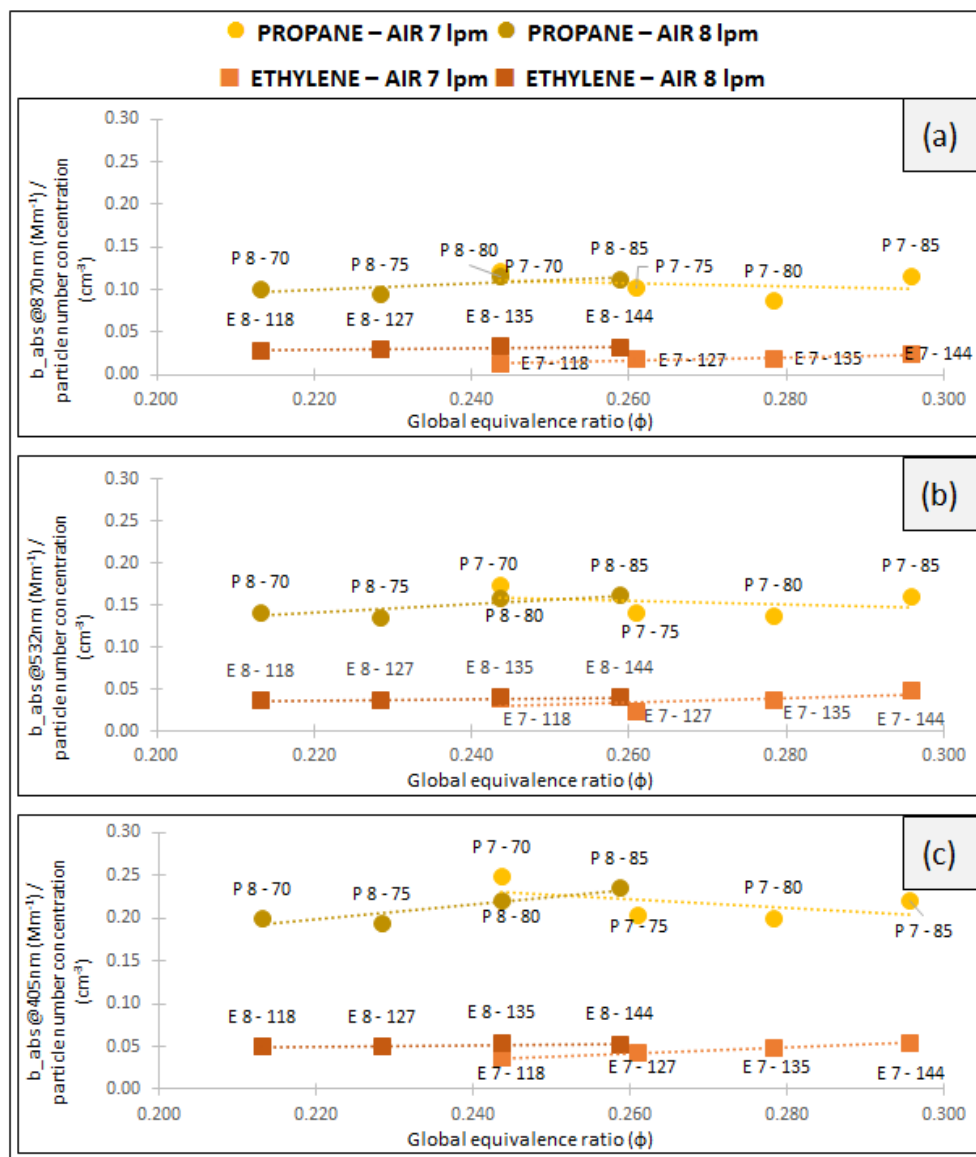
374

375 **3.2.4 Optical properties**

376 The optical properties of the MISG aerosol were determined in terms of the absorption coefficient (b_{abs} ;
377 i.e. the absorbance per unit length) (Massabò and Prati, 2021). The b_{abs} definition applies both to
378 measurements directly performed on the aerosol dispersed in the atmosphere (by PAXs, in this work) and to
379 off-line analyses on aerosol sampled on filters (by MWAA, in this work), provided a proper data reduction is
380 adopted (Massabò and Prati, 2021; and references therein).

381 The measured b_{abs} values were normalized to the total particle concentration inside ChAMBRé reached
382 in each single experiment. Absorption coefficients measured at three wavelengths by the PAXs and with the
383 cyclone mounted upstream, are shown in Fig. 11. Similar results were obtained even for experiments without
384 cyclone and for the b_{abs} values measured by the MWAA. At each wavelength, the b_{abs} values did not show
385 any dependence on the global equivalence ratio, with the propane producing particles more absorbent than
386 ethylene. The comparison with previous literature (Moallemi et al., 2019) is hampered by methodological
387 differences (Moallemi and co-workers used the IR PAX only and reported the Single Scattering Albedo instead
388 of the absorption coefficient).

389



390

391 *Figure 11: Absorption coefficient @ $\lambda = 870$ (a), 532 (b) and 405 (c) nm, measured by PAXs, versus the global*
 392 *equivalence ratio. b_{abs} values are normalized to the total particle number concentration measured by SMPS in the*
 393 *corresponding experiments. Each point is labelled by E or P (ethylene or propane) and a pair of numbers indicating air*
 394 *and fuel flow, respectively in lpm and mlpm.*

395

3.2.5 Mass Absorption Coefficient

396

The b_{abs} values, together with the EC concentration measured on the filter sampled during each single
 397 experiment, can be used to retrieve the Mass Absorption Coefficient (MAC) of the produced aerosol, through
 398 the relation:

398



399
$$b_{\text{abs}}(\lambda) = \text{MAC} * [\text{EC}]$$

400 where:

401 b_{abs} [Mm^{-1}]: absorption coefficient

402 MAC [$\text{m}^2 \text{g}^{-1}$]: Mass Absorption Coefficient

403 EC [$\mu\text{g m}^{-3}$]: Elemental Carbon concentration

404 The b_{abs} values were calculated directly online by the PAXs and offline by the MWAA analysis,
405 performed at five wavelengths on the sampled filters (see Sect. 2.5). This gave the possibility to extend the
406 characterization of the MISG and to compare two optical analyses on the same carbonaceous aerosol. Since
407 experiments were repeated with two different setups (i.e., with and without the cyclone) and two different fuels
408 (propane and ethylene), four different particle populations can be compared. The comparison was carried out
409 at the three wavelengths (nearly) common to PAXs and MWAA (i.e., $\lambda = 870/850, 532$ and 405 nm), as
410 reported in Fig. 11-13. We divided the results by fuel, air flow and with/without cyclone. Each point in the
411 plots sums-up the observations at different global equivalence ratio values.

412 The MWAA analysis at $\lambda = 870$ nm (Fig. 12.a) returns compatible MAC values for both the propane series
413 (with/without cyclone) and the ethylene series with cyclone (average MAC = $5.25 \pm 0.10 \text{ m}^2 \text{g}^{-1}$). At $\lambda = 532$
414 and 405 nm (Fig. 13.a and Fig. 14.a), propane series are still in agreement while the ethylene series with
415 cyclone show a higher MAC value (MAC = $9.53 \pm 0.08 \text{ m}^2 \text{g}^{-1}$ instead of MAC = $8.88 \pm 0.13 \text{ m}^2 \text{g}^{-1}$ at $\lambda = 532$
416 nm and MAC = $12.3 \pm 0.1 \text{ m}^2 \text{g}^{-1}$ instead of MAC = $10.7 \pm 0.2 \text{ m}^2 \text{g}^{-1}$ at $\lambda = 405$ nm). The ethylene series
417 without cyclone show consistent variability at all the three wavelengths, with the lowest MAC values of the
418 whole data-set (MAC = $3.78 \pm 0.08 \text{ m}^2 \text{g}^{-1}$; MAC = $5.9 \pm 0.1 \text{ m}^2 \text{g}^{-1}$; MAC = $6.9 \pm 0.1 \text{ m}^2 \text{g}^{-1}$ at $\lambda = 870, 532$
419 and 405 nm respectively): the differences are probably due to the production of super-micrometric particles
420 (see Sect 3.2.1 and Fig. 6) when the cyclone is not used. With the PAXs analysis (Fig. 12.b, 13.b and 14.b),
421 MAC values turn out higher in the series with cyclone (average values are MAC = $5.8 \pm 0.4 \text{ m}^2 \text{g}^{-1}$; $10.3 \pm$
422 $0.1 \text{ m}^2 \text{g}^{-1}$; $14 \pm 1 \text{ m}^2 \text{g}^{-1}$ at $\lambda = 870, 532$ and 405 nm respectively, with cyclone, MAC = $4.3 \pm 0.1 \text{ m}^2 \text{g}^{-1}$; 6.6
423 $\pm 1.7 \text{ m}^2 \text{g}^{-1}$; $8 \pm 2 \text{ m}^2 \text{g}^{-1}$ at $\lambda = 870, 532$ and 405 nm respectively, without cyclone), this happens at all the
424 three wavelengths and for both fuels. If series with cyclone are only considered, MAC values do not show any
425 significant differences depending on the fuel. The ethylene series without cyclone shows the lowest MAC
426 values at each wavelength, as observed with the MWAA analysis. PAXs data show a higher variability in
427 MAC values, likely due to a higher sensitivity to particle size than filter based MWAA analysis.

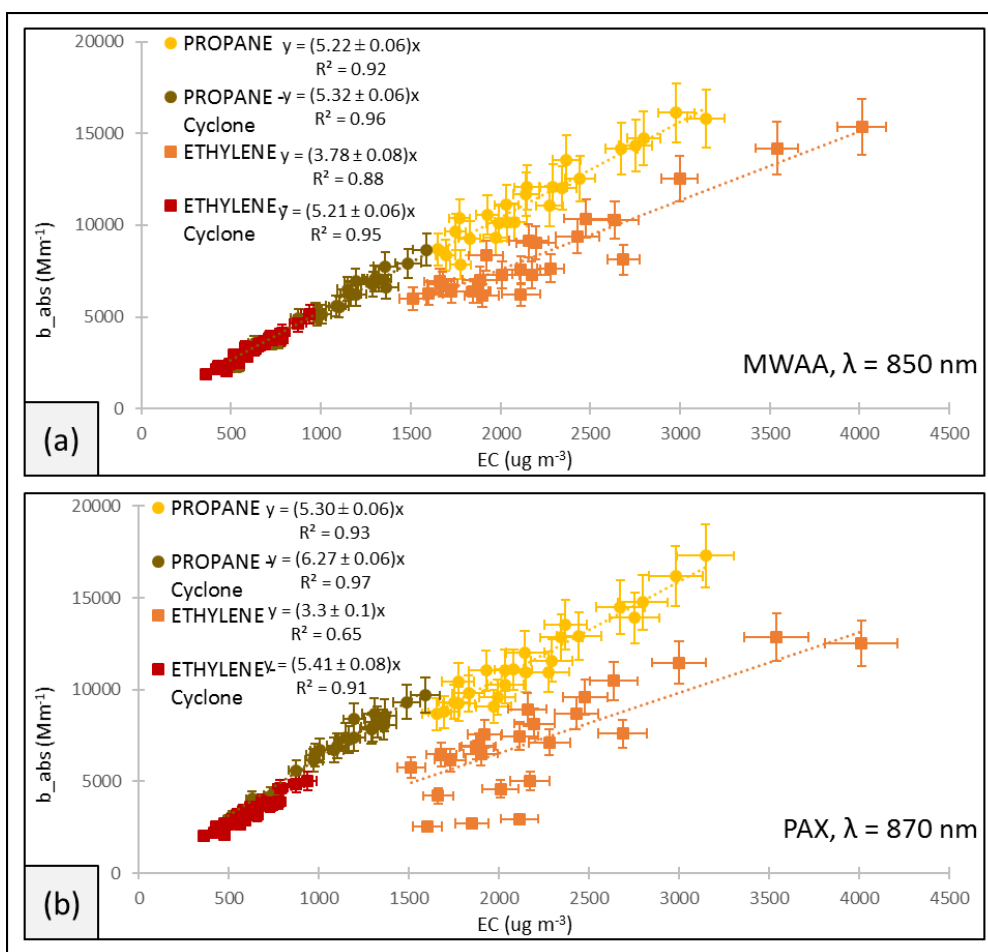
428

429

430

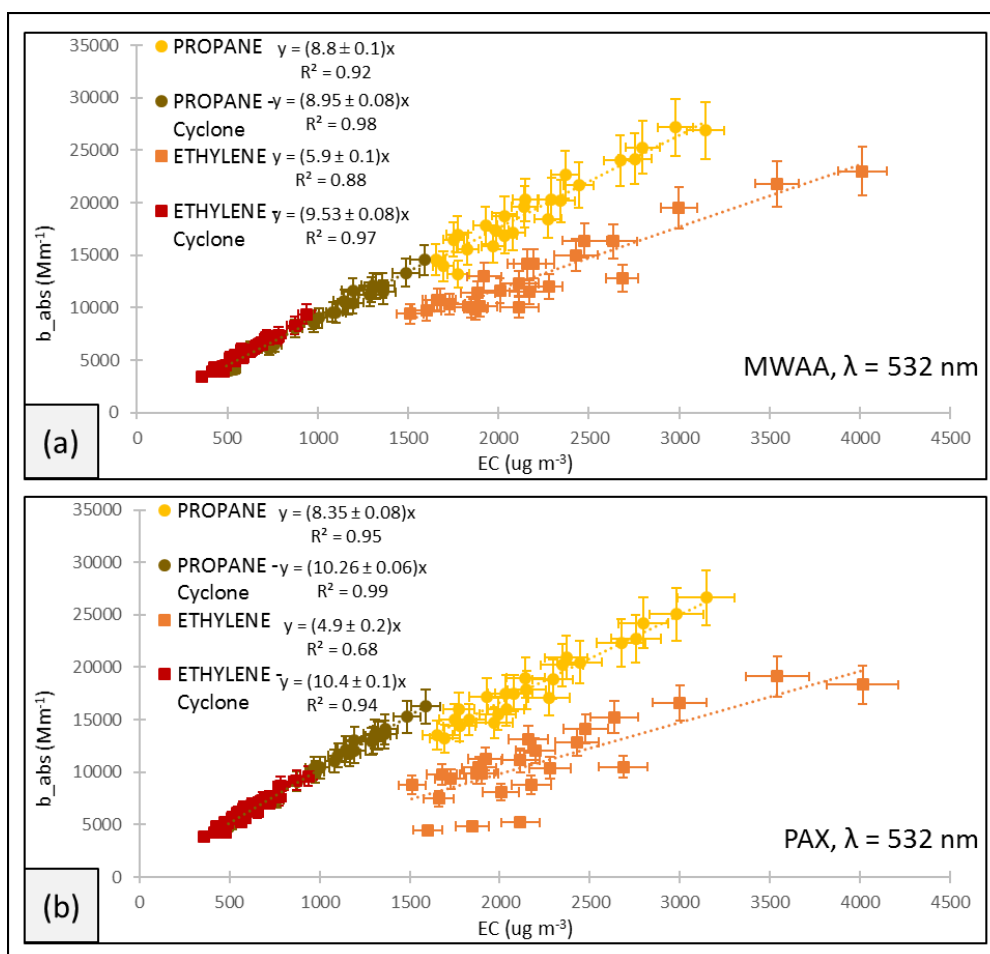
431

432



433

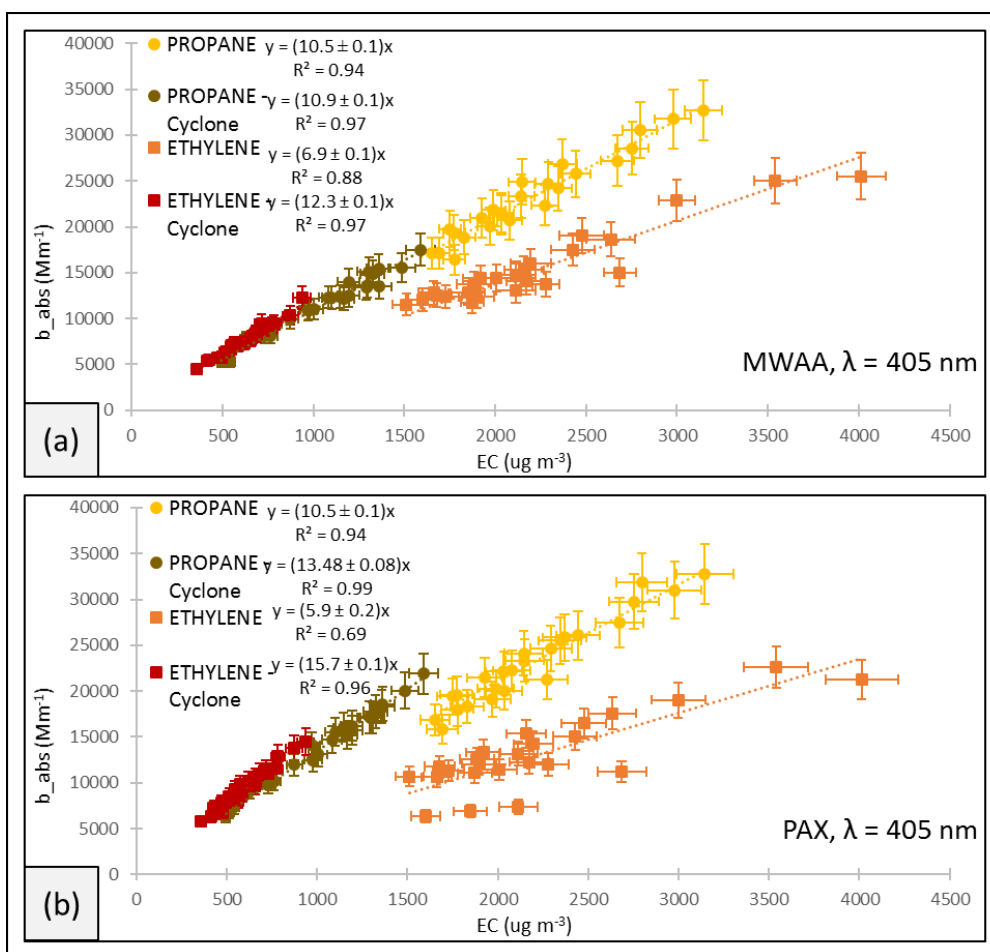
434 *Figure 12: Absorption coefficient at 850 nm measured by MWA (a) and @ 870 nm measured by PAX (b) versus EC*
435 *concentration. The slope of each fit corresponds to the Mass Absorption Coefficient.*
436



437

438 *Figure 13: Absorption coefficient @ 532 nm, measured by MWA (a) and PAX (b) versus EC concentration. The slope of*
439 *each fit corresponds to the Mass Absorption Coefficient.*

440



441

442 *Figure 14: Absorption coefficient at $\lambda = 405$ nm, measured by MWA (a) and PAX (b) versus EC concentration. The*
 443 *slope of each fit corresponds to the Mass Absorption Coefficient.*

444 A summary of all the measured MAC values, including the other two wavelengths available for the MWA
 445 (i.e., 635 and 375 nm) too, is given in Table 5. MAC values are close to theoretical figures for soot (Bond and
 446 Bergstrom, 2006), for both the fuels and at all the wavelengths. IR values are similar to those obtained by
 447 Moallemi (2019) for propane exhaust. With both the fuels MAC values increase when super-micrometric
 448 particles were removed by the cyclone; propane-particles showed higher MAC values than ethylene ones.

449

450

451

452

453



454

Table 5: Summary of the measured MAC values, in $\text{m}^2 \text{g}^{-1}$.

FUEL	PAX			MWAA				
	870 nm	532 nm	405 nm	850 nm	635 nm	532 nm	405 nm	375 nm
PROPANE	5.30 ± 0.06	8.35 ± 0.08	10.5 ± 0.1	5.22 ± 0.06	7.22 ± 0.09	8.8 ± 0.1	10.5 ± 0.1	10.9 ± 0.1
PROPANE with cyclone	6.27 ± 0.06	10.26 ± 0.06	13.48 ± 0.08	5.32 ± 0.06	7.37 ± 0.07	8.95 ± 0.08	10.9 ± 0.1	11.6 ± 0.1
ETHYLENE	3.3 ± 0.1	4.9 ± 0.2	5.9 ± 0.2	3.78 ± 0.08	5.0 ± 0.1	5.9 ± 0.1	6.9 ± 0.1	7.3 ± 0.1
ETHYLENE with cyclone	5.41 ± 0.08	10.4 ± 0.1	15.7 ± 0.1	5.21 ± 0.06	7.62 ± 0.07	9.53 ± 0.08	12.3 ± 0.1	13.0 ± 0.1

455

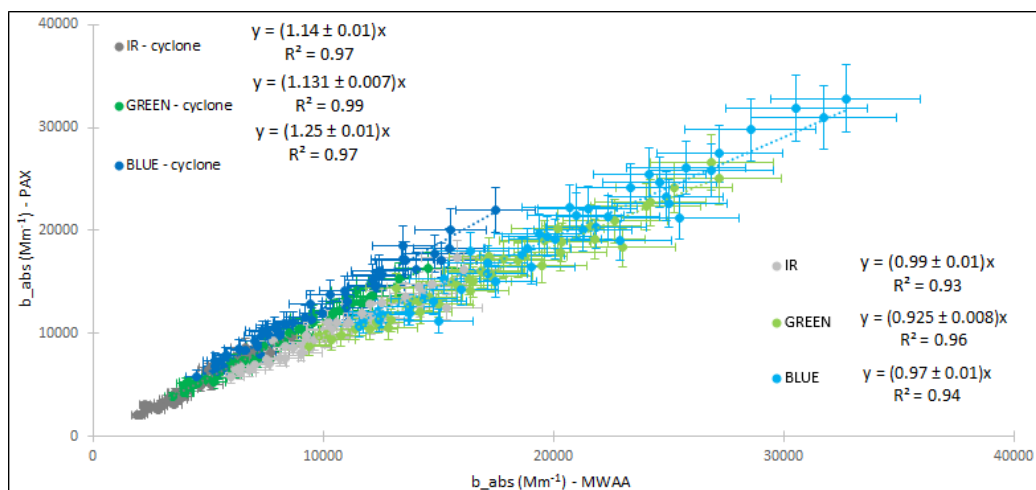
456

In (Moallemi et al., 2019) only IR-MAC values are reported for the propane and they resulted slightly lower than values here reported. This difference could depend on the different techniques used to quantify the EC concentration: we used EC concentration from thermal optical analysis while Moallemi (2019) used BC concentration measured by LII.

461

Discrepancies between MAC values obtained from PAXs and MWAA, for the same experiment, are compatible with the differences of measured b_{abs} values. The b_{abs} values measured by PAXs and MWAA are directly compared in Fig. 15, merging all the data collected by the two setups (i.e., with and without the cyclone) and for the two fuels. The agreement between the two analyses turned out within 25 % and 7 %, respectively without and with the cyclone.

466



467

Figure 15: Correlation study between the absorption coefficient measured by PAX and MWAA. Colours of identify the wavelength of the analysis: grey refers to 870 nm, green to 532 nm and blue to 405 nm; dark and light colours refer to experiments with and without cyclone, respectively.

471

In addition, the spectral dependence of the absorption coefficient b_{abs} , and consequently the Ångström Absorption Exponent (AAE, Moosmüller et al., 2011), can be calculated by the power-law:

473

$$b_{\text{abs}}(\lambda) \approx \lambda^{-\text{AAE}}$$

474 where:

475

b_{abs} [Mm^{-1}]: absorption coefficient

476

λ [nm]: wavelength used for the analysis

477

AAE: Ångström Absorption Exponent.



478 The averages of the resulting AAEs for the different experimental conditions are reported in Table 6.
479 Experimental determinations of the AAE had been reported in the literature as being dependent on aerosol
480 chemical composition (Kirchstetter et al., 2004; Utry et al., 2013) and size and morphology (Lewis et al., 2008;
481 Lack et al., 2012; Lack and Langridge, 2013; Filep et al., 2013; Utry et al., 2014 a). Particulate generated by
482 fossil fuel combustion (i.e., Black Carbon) typically has AAE values close to 1.0 (Harrison et al., 2013, and
483 references therein). The AAE values measured in this work for the MISG exhausts are generally close to 1.0
484 with higher figures for the cyclone-selected aerosol.

485

486 *Table 6: AAE values obtained in different experimental conditions through the analysis of PAXs MWAA raw data*

EXPERIMENTAL CONDITIONS	AAE - PAX	AAE - MWAA
PROPANE 70 to 85 mlpm - AIR 7 lpm	0.88 ± 0.06	0.92 ± 0.04
PROPANE 70 to 85 mlpm - AIR 8 lpm	0.92 ± 0.06	0.91 ± 0.05
PROPANE 70 to 85 mlpm - AIR 7 lpm - cyclone	0.98 ± 0.09	1.0 ± 0.1
PROPANE 70 to 85 mlpm - AIR 8 lpm - cyclone	1.05 ± 0.04	0.97 ± 0.09
ETHYLENE 118 to 144 mlpm - AIR 7 lpm	0.9 ± 0.3	0.84 ± 0.07
ETHYLENE 118 to 144 mlpm - AIR 8 lpm	0.76 ± 0.04	0.81 ± 0.06
ETHYLENE 118 to 144 mlpm - AIR 7 lpm - cyclone	1.40 ± 0.05	1.19 ± 0.09
ETHYLENE 118 to 144 mlpm - AIR 8 lpm - cyclone	1.39 ± 0.04	1.08 ± 0.05

487

488

489 4. Conclusion

490 A Mini-Inverted Soot Generator (MISG) was coupled with an atmospheric simulation chamber
491 (ChAMBRé) to compare the emissions of two fuels, ethylene, and propane. Different combustion conditions
492 (i.e., air and fuel flow, global equivalence ratio) were characterized in terms of size distribution, particle and
493 gas composition, optical properties, and EC concentration in the exhaust.

494 The MISG turned out to be a stable and reproducible soot particles source, suitable for experiments in
495 atmospheric simulation chambers. In addition, properties of emitted soot particles can be modulated by varying
496 the combustion conditions i.e., tuning the global equivalence ratio and/or varying the fuel used for combustion.

497 With equal conditions, ethylene combustion produces particles with higher number concentration and
498 smaller diameter than propane but is prone to generation of super-aggregates. These are likely formed directly
499 in the exhaust line where particles density is very high.

500 The carbonaceous compounds produced by propane are generally characterized by higher EC to TC ratios
501 than ethylene.

502 From the optical point of view, particles generated by propane turned out to be more light absorbing than
503 those formed by ethylene, although burning conditions (in terms of global equivalence ratio) were the same.
504 The values of the MAC parameter show a substantial agreement except those retrieved from the data collected
505 in the ethylene-no cyclone experiments. The latter resulted in lower MAC values, probably due to the presence
506 of super-aggregates in the chamber.

507 This work opens to new and more complex experiments. Well-characterized soot particles could be used to
508 investigate the effects that atmospheric parameters such as temperature and relative humidity can have on soot
509 particles, and also to study the interactions between soot particles and gaseous pollutants, solar radiation or
510 bio-aerosol.

511 Author contribution



512 VV and DM prepared the experimental setup, performed all the experiments and the data analysis; DM, FP,
513 and PP designed and built ChAMBRé; MB designed and implemented the acquisition software; VV and DM
514 prepared the article with contributions from the other authors.

515 **Competing interests**

516 The authors declare that they have no conflict of interest.

517 **Acknowledgments**

518 This project/work has received funding from the European Union's Horizon 2020 research and innovation
519 program through the EUROCHAMP-2020 Infrastructure Activity under grant agreement No 730997.

520 **References**

521 Ackerman, A., Toon, O., Stevens, D., Heymsfield, A., Ramanathan, V., and Welton, E.: Reduction of tropical
522 cloudiness by soot, *Science*, 288(5468), 1042–1047, doi:10.1126/science.288.5468.1042, 2000.

523 Anenberg, S. C., Horowitz, L. W., Tong, D. Q., and West, J. J.: An estimate of the global burden of
524 anthropogenic ozone and fine particulate matter on premature human mortality using atmospheric modelling,
525 *Environ. Health Perspec.*, 118 (9):1189–95, doi:10.1289/ehp.0901220, 2010.

526 Baccolo, G., Nastasi, M., Massabò, D., Clason, C., Di Mauro, B., Di Stefano, E., Łokas, E., Prati, P., Previtali,
527 E., Takeuchi, N., Delmonte, B., Maggi, V.: Artificial and natural radionuclides in cryoconite as tracers of
528 supraglacial dynamics: Insights from the Morteratsch glacier (Swiss Alps), *CATENA*, 191:104577,
529 10.1016/j.catena.2020.104577, 2020.

530 Becker, K. H. (2006): Overview on the Development of Chambers for the Study of Atmospheric Chemical
531 Processes, in: *Environmental Simulation Chambers: Application to Atmospheric Chemical Processes*, edited
532 by: Barnes I. and Rudzinski K. J., Springer, Amsterdam, 1–26.

533 Bescond, A., Yon, J., Ouf, F. X., Roze, C., Coppalle, A., Parent, P., Ferry, D., and Laffon, C.: Soot optical
534 properties determined by analyzing extinction spectra in the visible near-UV: Toward an optical speciation
535 according to constituents and structure, *J. Aerosol Sci.* 101:118–32, doi:10.1016/j.jaerosci.2016.08.001, 2016.

536 Birch, M. E. and Cary, R. A.: Elemental carbon-based method for occupational monitoring of particulate diesel
537 exhaust: methodology and exposure issues, *Analyst*, 121, 1183–1190, 1996.

538 Bischof, O. F., Weber, P., Bundke, U., Petzold, A., and Kiendler-Scharr, A.: Characterization of the
539 Miniaturized Inverted Flame Burner as a Combustion Source to Generate a Nanoparticle Calibration Aerosol,
540 *Emission Contr. Sci. Technol.* 6:37-46, DOI: 10.1007/s40825-019-00147-w, 2019.

541 Bond, T. C., and Bergstrom, R. W.: Light Absorption by Carbonaceous Particles: An Investigative Review,
542 *Aerosol Science and Technology*, 40:1, 27-67, DOI: 10.1080/02786820500421521, 2006.

543 Bond, T. C., Doherty, S. J., Fahey, D. W., Forster, P. M., Berntsen, T., De Angelo, B. J., et al.: Bounding the
544 role of black carbon in the climate system: A scientific assessment, *Journal of Geophysical Research*
545 *Atmospheres*, 118(11), 5380–5552. <https://doi.org/10.1002/jgrd.50171>, 2013.

546 Caponi, L., Formenti, P., Massabó, D., Di Biagio, C., Cazaunau, M., Pangui, E., Chevallier, S., Landrot, G.,
547 Andreae, M. O., Kandler, K., Piketh, S., Saeed, T., Seibert, D., Williams, E., Balkanski, Y., Prati, P., and



- 548 Doussin, J.-F.: Spectral- and size-resolved mass absorption efficiency of mineral dust aerosols in the shortwave
549 spectrum: a simulation chamber study, *Atmos. Chem. Phys.*, 17, 7175–7191, [https://doi.org/10.5194/acp-17-](https://doi.org/10.5194/acp-17-7175-2017)
550 [7175-2017](https://doi.org/10.5194/acp-17-7175-2017), 2017.
- 551 Cassee, F. R., Héroux, M. E., Gerlofs-Nijland, M. E., and Kelly, F. J.: Particulate matter beyond mass: Recent
552 health evidence on the role of fractions, chemical constituents and sources of emission, *Inhalation Toxicology*,
553 25(14), 802–812. <https://doi.org/10.3109/08958378.2013.850127>, 2013.
- 554 Cross, E. S., T. B. Onasch, T. B., Ahern, A., Wrobel, W., Slowik, J. G., Olfert, J., Lack, D. A., Massoli, P.,
555 Cappa, C. D., Schwarz, J. P., et al.: Soot particle studies-instrument inter-comparison-project overview,
556 *Aerosol Sci. Technol.*, 44 (8):592–611. doi:10.1080/02786826.2010.482113, 2010.
- 557 Danelli, S. G., Brunoldi, M., Massabò, D., Parodi, F., Vernocchi, V., and Prati, P.: Comparative
558 characterization of the performance of bio-aerosol nebulizers in connection with atmospheric simulation
559 chambers, *Atmos. Meas. Tech.*, 14, 4461–4470, <https://doi.org/10.5194/amt-14-4461-2021>, 2021.
- 560 Durdina, L., Lobo, P., Trueblood, M. B., Black, E. A., Achterberg, S., Hagen, D. E., Brem, B. T., and Wang,
561 J.: Response of real-time black carbon mass instruments to mini-CAST soot, *Aerosol Sci. Technol.* 50 (9):
562 906–18, doi: 10.1080/02786826.2016.1204423, 2016.
- 563 Filep, Á., Ajtai, T., Utry, N., Pintér, M. D., Nyilas, T., Takács, S., Máté, Z., Gelencsér, A., Hoffer, A.,
564 Schnaiter, M., Bozóki, Z., and Szabó, G.: Absorption spectrum of ambient aerosol and its correlation with size
565 distribution in specific atmospheric conditions after a red mud accident, *Aerosol Air Qual. Res.*, 13, 49–59,
566 2013.
- 567 Finlayson-Pitts, B. J. and Pitts Jr., J. N.: *Chemistry of the upper and lower atmosphere: Theory, experiments*
568 *and applications*, Academic Press, San Diego, CA, 2000.
- 569 Gan, W. Q., Koehoorn, M., Davies, H. W., Demers, P. A., Tamburic, L., and Brauer, M.: Long-term exposure
570 to traffic-related air pollution and the risk of coronary heart disease hospitalization and mortality,
571 *Environmental Health Perspectives*, 119(4), 501–507, <https://doi.org/10.1289/ehp.1002511>, 2011.
- 572 Ghazi, R., and Olfert, J. S.: Coating mass dependence of soot aggregate restructuring due to coatings of oleic
573 acid and dioctyl sebacate, *Aerosol Sci. Technol.* 47 (2):192–200. doi:10.1080/02786826.2012.741273, 2013.
- 574 Ghazi, R., Tjong, H., Soewono, A., Rogak, S. N., and Olfert, J. S.: Mass, mobility, volatility, and morphology
575 of soot particles generated by a McKenna and inverted burner, *Aerosol Sci. Technol.* 47 (4):395–405.
576 doi:10.1080/02786826.2012.755259, 2013.
- 577 Harrison, R. M., Beddows, D. C. S., Jones A. M., Calvo A., Alves C., and Pio C.: An evaluation of some issues
578 regarding the use of aethalometers to measure woodsmoke concentrations, *Atmos. Environ.*, 80, 540–548,
579 2013.
- 580 Henning, S., Ziese, M., Kiselev, A., Saathoff, H., Möhler, O., Mentel, T. F., Buchholz, A., Spindler, C.,
581 Michaud, V., Monier, M., et al.: Hygroscopic growth and droplet activation of soot particles: Uncoated,
582 succinic or sulfuric acid coated, *Atmos. Chem. Phys.* 12 (10):4525–37. doi: 10.5194/acp-12-4525-2012, 2012.
- 583 Janssen, N., Gerlofs-Nijland, M., Lanki, T., Salonen, R., Cassee, F., Hoek, G., Fischer, P., Brunekreef, B., and
584 Krzyzanowski, M.: *Health effects of black carbon*, Res. Rep., World Health Organization, Regional Office for
585 Europe, Copenhagen, Denmark, 2012



- 586 Kazemimanesh, M., Moallemi, A., Thomson, K., Smallwood, G., Lobo, P., and Olfert, J. S.: A novel miniature
587 inverted-flame burner for the generation of soot nanoparticles, *Aerosol Science and Technology*, 53 (2), 184-
588 195, [10.1080/02786826.2018.1556774](https://doi.org/10.1080/02786826.2018.1556774), 2019.
- 589 Kirchstetter, T. W., Novakok, T., and Hobbs, P. V.: Evidence that the spectral dependence of light absorption
590 by aerosols is affected by organic carbon, *J. Geophys. Res.*, 109, D21208,
591 <https://doi.org/10.1029/2004JD004999>, 2004.
- 592 Kumar, N. K., Corbin, J. C., Bruns, E. A., Massabò, D., Slowik, J. G., Drinovec, L., Močnik, G., Prati, P.,
593 Vlachou, A., Baltensperger, U., Gysel, M., El-Haddad, I., and Prévôt, A. S. H.: Production of particulate brown
594 carbon during atmospheric aging of residential wood-burning emissions, *Atmos. Chem. Phys.*, 18, 17843–
595 17861, <https://doi.org/10.5194/acp-18-17843-2018>, 2018.
- 596 Lack, D. A. and Langridge, J. M.: On the attribution of black and brown carbon light absorption using the
597 Ångström exponent, *Atmos. Chem. Phys.*, 13, 10535–10543, <https://doi.org/10.5194/acp-13-10535-2013>,
598 2013.
- 599 Lack, D. A., Langridge, J. M., Bahreini, R., Cappa, C. D., Middlebrook, A. M., and Schwarz, J. P.: Brown
600 carbon and internal mixing in biomass burning particles, *P. Natl. Acad. Sci. USA*, 109, 14802–14807, 2012.
- 601 Lelieveld, J., Evans, J. S., Fnais, M., Giannadaki, D., and Pozzer, A.: The contribution of outdoor air pollution
602 sources to premature mortality on a global scale, *Nature* 525 (7569):367–71. doi:10.1038/nature15371, 2015.
- 603 Lewis, K., Arnott, W. P., Moosmüller, H., and Wold, C. E.: Strong spectral variation of biomass smoke light
604 absorption and single scattering albedo observed with a novel dual-wavelength photoacoustic instrument, *J.*
605 *Geophys. Res.*, 113, D16203, <https://doi.org/10.1029/2007JD009699>, 2008.
- 606 Mamakos, A., Khalek, I., Giannelli, R., and Spears, M.: Characterization of Combustion Aerosol Produced by
607 a Mini-CAST and Treated in a Catalytic Stripper, *Aerosol Science and Technology*, 47:8, 927-936,
608 DOI:10.1080/02786826.2013.802762, 2013.
- 609 Massabò, D., and Prati P.: An overview of optical and thermal methods for the characterization of
610 carbonaceous aerosol, *La Rivista del Nuovo Cimento*, vo. 44:3, DOI: 10.1007/s40766-021-00017-8, 2021.
- 611 Massabò, D., Prati, P., Canepa, E., Bastianini, M., Van Eijk, A.M.J., Missamou, T., Piazzola, J.:
612 Characterization of carbonaceous aerosols over the Northern Adriatic Sea in the JERICO-NEXT project
613 framework, *Atmospheric Environment*, 228:117449, DOI: 10.1016/j.atmosenv.2020.117449, 2020.
- 614 Massabò, D., Altomari, A., Vernocchi, V., and Prati, P.: Two-wavelength thermal–optical determination of
615 light-absorbing carbon in atmospheric aerosols, *Atmos. Meas. Tech.*, 12, 3173–3182,
616 <https://doi.org/10.5194/amt-12-3173-2019>, 2019.
- 617 Massabò, D., Danelli S. G., Brotto P., Comite A., Costa C., Di Cesare A., Doussin J. F., Ferraro F., Formenti
618 P., Gatta E., Negretti L., Oliva M., Parodi F., Vezzulli L., and Prati P.: ChAMBRé: a new atmospheric
619 simulation chamber for aerosol modelling and bioaerosol research, *Atmos. Meas. Tech.* 11, 5885-5900, 2018.
- 620 Massabò, D., Caponi, L., Bove, M. C., and Prati, P.: Brown carbon and thermal-optical analysis: a correction
621 based on optical multiwavelength apportionment of atmospheric aerosols, *Atmos. Environ.*, 125, 119–125,
622 2016. <https://doi.org/10.1016/j.atmosenv.2015.11.011>
- 623 Massabò, D., Caponi, L., Bernardoni, V., Bove, M. C., Brotto, P., Calzolari, G., Cassola, F., Chiari, M., Fedi,
624 M. E., Fermo, P., Giannoni, M., Lucarelli, F., Nava, S., Piazzalunga, A., Valli, G., Vecchi, R., and Prati, P.:



- 625 Multi-wavelength optical determination of black and brown carbon in atmospheric aerosols, *Atmos. Environ.*,
626 108, 1–12, 2015.
- 627 Menon, S., Hansen, J., Nazarenko, L., and Luo, Y.: Climate effects of black carbon aerosols in China and
628 India, *Science* 297 (5590):2250–53. doi:10.1126/science1075159, 2002.
- 629 Moallemi, A., Kazemimanesh, M., Corbin, J. C., Thomson, K., Smallwood, G., Olfert, J. S., and Lobo, P.:
630 Characterization of black carbon particles generated by a propane-fueled miniature inverted soot generator,
631 *Journal of Aerosol Science*, 135, 46–57, 10.1016/j.jaerosci.2019.05.004, 2019.
- 632 Moore R. H., Ziemba L. D., Dutcher D., Beyersdorf A. J., Chan K., Crumeyrolle S., Raymond T. M., Thornhill
633 K. L., Winstead E. L. and Anderson B. E.: Mapping the Operation of the Miniature Combustion Aerosol
634 Standard (Mini-CAST) Soot Generator, *Aerosol Science and Technology*, 48:5, 467–479, DOI:
635 10.1080/02786826.2014.890694, 2014.
- 636 Moosmüller, H., Chakrabarty, R.K., Ehlers, K.M., Arnott, W.P.: Absorption Ångström coefficient, brown
637 carbon, and aerosols: basic concepts, bulk matter, and spherical particles. *Atmos. Chem. Phys.* 11, 1217e1225,
638 2011.
- 639 Moschos, V., Gysel-Beer, M., Modini, R. L., Corbin, J. C., Massabò, D., Costa, C., Danelli, S. G., Vlachou,
640 A., Daellenbach, K. R., Szidat, S., Prati, P., Prévôt, A. S. H., Baltensperger, U., and El Haddad, I.: Source-
641 specific light absorption by carbonaceous components in the complex aerosol matrix from yearly filter-based
642 measurements, *Atmos. Chem. Phys.*, 21, 12809–12833, <https://doi.org/10.5194/acp-21-12809-2021>, 2021.
- 643 NIOSH: Method 5040 Issue 3: Elemental Carbon (Diesel Exhaust). In *NIOSH Manual of Analytical Methods*.
644 National Institute of Occupational Safety and Health, Cincinnati, OH, 1999.
- 645 Nordmann, S., Birmili, W., Weinhold, K., Müller, K., Spindler, G., and Wiedensohler, A.: Measurements of
646 the mass absorption cross section of atmospheric soot particles using Raman spectroscopy, *J. Geophys. Res.*
647 *Atmos.*, 118, 12,075–12,085, doi: 10.1002/2013JD020021, 2013.
- 648 Onasch, T. B., Trimborn, A., Fortner, E. C., Jayne, J. T., Kok, G. L., Williams, L. R., Davidovits, P. and
649 Worsnop, D. R.: Soot particle aerosol mass spectrometer: Development, validation, and initial application,
650 *Aerosol Sci. Technol.* 46 (7):804–17, doi:10.1080/02786826.2012.663948, 2012.
- 651 Pagels, J., Khalizov, A. F., McMurry, P. H., and Zhang, R. Y.: Processing of soot by controlled sulphuric acid
652 and water condensation—Mass and mobility relationship, *Aerosol Sci. Technol.* 43 (7):629–4,
653 doi:10.1080/02786820902810685, 2009.
- 654 Petzold, A., Ogren, J. A., Fiebig, M., Laj, P., Li, S.-M., Baltensperger, U., Holzer-Popp, T., Kinne, S.,
655 Pappalardo, G., Sugimoto, N., Wehrli, C., Wiedensohler, A., and Zhang, X.-Y.: Recommendations for
656 Reporting “Black Carbon”, *Measurements. Atmos. Chem. Phys.*, 13:8365–8379, 2013.
- 657 Petzold, A., Schloesser, H., Sheridan, P.J., Arnott, W.P., Ogren, J.A., Virkkula, A.: Evaluation of multiangle
658 absorption photometry for measuring aerosol light absorption, *Aerosol Sci. Technol.* 39 (1), 2005.
- 659 Petzold, A., and Schöllner, M.: Multi-angle absorption photometry—a new method for the measurement of
660 aerosol light absorption and atmospheric black carbon, *Journal of Aerosol Science*, 35, 421–441, 2004.
- 661 Pope, C.A. III, Burnett, R. T., Thun, M. J., Calle, E. E., Krewski, D., Ito, K., et al.: Lung Cancer,
662 Cardiopulmonary Mortality, and Long-term Exposure to Fine Particulate Air Pollution. *J. Am. Med. Assoc.*,
663 287(9):1132–41, 2002.



- 664 Quinn, P. K., Bates, T. S., Baum, E., Doubleday, N., Fiore, A. M., Flanner, M., et al.: Short-lived pollutants in
665 the Arctic: Their climate impact and possible mitigation strategies, *Atmospheric Chemistry and Physics*, 8(6),
666 1723–1735. <https://doi.org/10.5194/acp-8-1723-2008>, 2008.
- 667 Ramanathan, V., and G. Carmichael, G.: Global and regional climate changes due to black carbon, *Nat. Geosci.*
668 1 (4):221–27. doi:10.1038/ngeo156, 2008.
- 669 Saturno, J., Pöhlker, C., Massabò, D., Brito, J., Carbone, S., Cheng, Y., Chi, X., Ditas, F., Hrabě de Angelis,
670 I., Morán-Zuloaga, D., Pöhlker, M. L., Rizzo, L. V., Walter, D., Wang, Q., Artaxo, P., Prati, P., and Andreae,
671 M. O.: Comparison of different Aethalometer correction schemes and a reference multi-wavelength absorption
672 technique for ambient aerosol data, *Atmos. Meas. Tech.*, 10, 2837–2850, [https://doi.org/10.5194/amt-10-2837-](https://doi.org/10.5194/amt-10-2837-2017)
673 2017, 2017.
- 674 Scerri, M. M., Kandler, K., Weinbruch, S., Yubero, E., Galindo N., Prati, P., Caponi, L., and Massabò, D.:
675 Estimation of the contributions of the sources driving PM_{2.5} levels in a Central Mediterranean coastal town,
676 *Chemosphere*, 211, 465–481, <https://doi.org/10.1016/j.chemosphere.2018.07.104>, 2018.
- 677 Stipe, C. B., Higgins, B. S., Lucas, D., Koshland, C. P., & Sawyer, R. F. Inverted co-flow diffusion flame for
678 producing soot, *Review of Scientific Instruments*, 76 (2), <https://doi.org/10.1063/1.1851492>, 2005.
- 679 Utry, N., Ajtai, T., Filep, Á., Dániel P. M., Hoffer, A., Bozoki, Z., and Szabó, G.: Mass specific optical
680 absorption coefficient of HULIS aerosol measured by a four-wavelength photoacoustic spectrometer at NIR,
681 VIS and UV wavelengths, *Atmos. Environ.*, 69, 321–324, 2013.
- 682 Utry, N., Ajtai, T., Filep, Á., Pintér, M., Török, Zs., Bozóki, Z., and Szabó, G.: Correlations between absorption
683 Angström exponent (AAE) of wintertime ambient urban aerosol and its physical and chemical properties,
684 *Atmos. Environ.*, 91, 52–59, 2014.
- 685 Utry, N., Ajtai, T., Pinter, M., Bozóki, Z., and Szabó, G.: Wavelength-dependent optical absorption properties
686 of artificial and atmospheric aerosol measured by a multiwavelength photoacoustic spectrometer. *Int. J.*
687 *Thermophys.*, 35 (12):2246–58. doi:10.1007/s10765-014-1746-6, 2014
- 688 von der Weiden, S.-L., Drewnick, F., and Borrmann, S.: Particle Loss Calculator – a new software tool for the
689 assessment of the performance of aerosol inlet systems, *Atmos. Meas. Tech.*, 2, 479–494,
690 <https://doi.org/10.5194/amt-2-479-2009>, 2009.
- 691 Weijer, E. P., Schaap, M., Nguyen, L., Matthijsen, J., Denier van der Gon, H. A. C., et al.: Anthropogenic and
692 Natural Constituents in Particulate Matter in the Netherlands, *Atmos. Chem. Phys.*, 11:2281–2294, 2011.
- 693 Zhang, R., Khalizov, A. F., Pagels, J., Zhang, D., Xue, H., and McMurry, P. H.: Variability in morphology,
694 hygroscopicity, and optical properties of soot aerosols during atmospheric processing, *Proc. Natl. Acad. Sci.*
695 *USA* 105 (30):10291–96. doi:10.1073/pnas.0804860105, 2008.